Multi-Stencil Streamline Fast Marching: a general 3D Framework to determine Myocardial Thickness and Transmurality in Late Enhancement Images

Susana Merino-Caviedes, Lucilio Cordero-Grande, Ana Revilla-Orodea, Teresa Sevilla-Ruiz, M. Teresa Pérez, Marcos Martín-Fernández and Carlos Alberola-López, *Senior Member, IEEE*

Abstract

We propose a fully three-dimensional methodology for the computation of myocardial non-viable tissue transmurality in contrast enhanced magnetic resonance images. The outcome is a continuous map defined within the myocardium where not only current state-of-the-art measures of transmurality can be calculated, but also information on the location of non-viable tissue is preserved. The computation is done by means of a partial differential equation framework we have called Multi-Stencil Streamline Fast Marching (MSSFM). Using it, the myocardial and scarred tissue thickness is simultaneously computed. Experimental results show that the proposed 3D method allows for the computation of transmurality in myocardial regions where current 2D methods are not able to as conceived, and it also provides more robust and accurate results in situations where the assumptions on which current 2D methods are based —i.e., there is a visible endocardial contour and its corresponding epicardial points lie on the same slice—, are not met.

Index Terms

Perfusion imaging, heart, quantification and estimation, myocardial viability, transmurality, fast marching.

 Digital Object Identifier 10.1109/TMI.2013.2276765.

This work was partially supported by the Spanish Ministerio de Ciencia e Innovación and the Fondo Europeo de Desarrollo Regional under Research Grant TEC2010-17982, the Spanish Instituto de Salud Carlos III under Research Grant PI11–01492, the European Commission under Research Grant FP7-223920 and the Spanish Centro para el Desarrollo Tecnológico Industrial (CDTI) under the cvREMOD project and Research Grant CEN-20091044. The work was also funded by the Spanish Junta de Castilla y León under Grants VA039A10–2, VA376A11-2, GRS 474/A/10, SAN103/VA40/11, SAN126/VA032/09 and SAN126/VA033/09.

S. Merino-Caviedes, L. Cordero-Grande, M. Martín-Fernández and C. Alberola-López are with the Laboratorio de Procesado de Imagen of the Universidad de Valladolid. E-mail: smercav@lpi.tel.uva.es

A. Revilla-Orodea and T. Sevilla-Ruiz are with the Servicio de Cardiología, Hospital Clínico Universitario, Valladolid, Spain.

M. T. Pérez is with the Departamento de Matemática Aplicada of the Universidad de Valladolid.

I. Introduction

According to the World Health Organization, cardiovascular diseases are the leading cause of death in the world and, among them, ischemic heart disease (IHD) was in 2008 the most prevalent in middle- and high-income countries [1], [2]. IHD shows up as a restriction of blood supply that may cause damage to myocardial tissue due to oxygen shortage.

Among the existing cardiac magnetic resonance (CMR) modalities that are employed in clinical practice, Contrast Enhanced (CE) CMR imaging is able to detect infarcted tissue in the myocardium by highlighting regions with contrast accumulation [3]. In this modality, a metabolically inert paramagnetic contrast bolus, usually composed of a Gadolinium Chelate, is injected into the patient. The volumes are acquired when the contrast has been washed out of the myocardial viable tissue, but it is still present in the damaged tissue due to a number of reasons [4]: low perfusion, fibrosis, inflammation or tumor neovasculature. This causes the damaged tissue to appear hyperenhanced in the image, since the paramagnetic contrast shortens the T1 relaxation time. Therefore, CE-CMR is of great interest in IHD, as well as in several non-ischemic pathologies such as myocarditis or hypertrophic cardiomyopathy (HCM) [5] [6].

About IHD, it is well known that some of the affected myocardium may recover its functionality by revascularization if there is viable tissue [7]. The transmural extent of the damaged tissue is often used as a relevant criterion to decide the appropriateness of a revascularization procedure [4], [8]–[10]: if the non-viable tissue covers more than 50% of the myocardial wall thickness, it is unlikely that the contractile function will be recovered [4]. Regarding other non-ischemic cardiomyopathies, it has been described [11] that 26% to 75% of scarred wall thickness is significantly predictive of inducible ventricular tachycardia (VT). The authors include in their study numerous cases with non-subendocardial scar as it is frequently the case in this sort of cardiomyopathies. This suggests that an accurate framework to measure thickness and transmurality seems beneficial towards a detailed diagnostic procedure for both ischemic and non-ischemic cardiomyopathies.

In cardiomyopathies, VT may appear due to the existence of functional tissue islands surrounded by non-viable myocardium [12]. Besides implantable cardioverter-defibrillators, catheter ablation is an important tool for the treatment of this pathology [13]; this technique is based on removing conducting channels (CC) by damaging the arrhytmogenic substrate present at any depth in the myocardium, and it may be performed through an intracardiac or percutaneous approach. In that respect, the development of tools to assist in the decision of which approach to choose might be helpful in clinical practice. To guide the ablation procedure and to identify existing CC, an electroanatomic voltage map is created by a point-by-point probing of the endocardium, which is a time-consuming and invasive task. Moreover, it provides only a rough delineation of scar areas in the basal septum and posterior wall of the left ventricle due to the difficulty in accessing them in a trans-aortic catheterism [14].

Sustained monomorphic VT substrate has been noninvasively identified by channels of heterogeneous tissue (HT) in CE-CMR images [15]–[17]. In [18], high-resolution CE-CMR images were integrated into a CARTO navigation system to aid the VT ablation procedure, and the authors also reported a good correlation between the endocardial

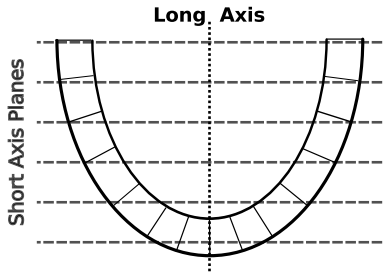

Figure 1. Example of the crossing of SA planes within an LA slice. Some endocardial-epicardial point-to-point correspondences are depicted.

electroanatomic maps and a projection into the endocardium of the scar present at the subendocardial half-wall of the myocardium, segmented from the CE-CMR image. Therefore, having a precise map of scar location and layout seems of great interest in this application domain as well to shift from invasive to non-invasive clinical procedures.

A. Existing Methods for Transmurality Computation

Several methods for computing scar transmurality in two-dimensional CE-CMR slices have been reported in the literature, most of them following a ray-tracing methodology [11], [19], [20]. They start by dividing the myocardium into sectors and tracing paths along which the amount of myocardial and scarred tissue is computed. The transmurality on each path is computed and the transmurality measures are finally averaged within each myocardial sector. A summary of the main differences among these methods is shown in Table I; they mainly stem from how paths are chosen and how tissue thickness is computed.

Specifically, in Schuijf et al. [19], a modification of the centerline method [21] was used, where the myocardium and scar thickness were evaluated along 100 rays and the myocardium was sampled with 10 points per ray to compute the transmurality as the average of sampled points belonging to non-viable tissue. Nazarian et al. [11] employed 30 radial lines per each of the 12 sectors which the myocardium was partitioned into. Tissue thickness was defined as the length of the segment between the starting and the ending points belonging to the tissue in the path. Recently, Elnakib et al. [20] used point-to-point correspondences between the endocardial and epicardial contours, found by solving a two-dimensional Laplace equation in the myocardium, and computing the streamlines out of the solution. The sectors were assigned following the 17-segment myocardium model [22]. The Laplace partial differential equation (PDE) has been previously employed as a means to compute the thickness of the highly geometrically irregular human brain cortex [23], [24]. A different approach was shown in [10] where, instead of using a ray tracing approach, the sector transmurality was given by dividing the scar tissue area by the whole sector area.

These methods are devised for two-dimensional image slices, mostly short-axis (SA) acquisitions, although [19] and [20] may be applied to long-axis (LA) slices as well. In particular, [11] implicitly assumes that the endo- and epicardial contours can be modeled as two concentric circumferences, an assumption that does not hold on LA acquisitions or in certain heart diseases such as HCM, where there is a significant thickening of part of the heart

Table I

COMPARISON OF THE TRANSMURALITY METHODS IN THE LITERATURE AND THE PROPOSED ONE.

Method	Schuijf et al. [19]	Nazarian et al. [11]	Elnakib et al. [20]	Proposed
Dimension	2D	2D	2D	2D, 3D
Chosen paths	Centerline normals	Radial lines	Streamlines	Streamlines
Thickness computation	Point sampling	Segment length	Segment length	Line integral
Need of explicit lines	Yes	Yes	Yes	No
Location information	No	No	No	Yes
Soft segmentations	No	Yes	No	Yes

muscle. They also need both the endocardium and the epicardium to be visible in the slices where transmurality is to be computed, which might not be necessarily the case in SA apical slices (see Figure 1). Also, the endocardial-epicardial point correspondences may not be located within the same 2D slice. Figure 1 shows that the closer to the apex, the further apart these points are located in the LA direction. In addition, none of these methods keeps information about the scar depth location although such a piece of information might be useful to distinguish between epicardial and endocardial scars, for example in determining whether an epicardial or an endocardial approach would be best. It must be noted that the methods relying on measuring segment lengths assume that all the scar within the myocardial path is compact with no healthy tissue in-between, which is the case in IHD but may not be in other pathologies. Two possibilities not taken into account are that a highly transmural scar island may be distributed into neighboring sectors, or the presence of fibrotic tissue in islands within a sector. Because of the averaging and depending on how much healthy tissue remains within each sector, these sectors may yield a much lower transmurality than what would be clinically expected. In such cases, averaging by sectors hides the underlying scar distribution, while a local transmurality map would disclose it. In addition, such a local map would remain unaffected by described discrepancies between sectors and actual coronary layout [25].

B. Contributions and Paper Structure

In this paper, we propose a dense transmurality map which is, to the best of our knowledge, the first fully 3D transmurality method that takes into account the patient-specific myocardial geometry and that provides partial measures of the subendocardial transmurality at every point of the myocardium. In order to accomplish this, an Eulerian algorithm that simultaneously computes scar and myocardial thickness maps has been developed by means of a Multi-Stencil Streamline Fast Marching (MSSFM) method. While the image data set used in this paper consists of CE-CMR volumes, the proposed methodology is not restricted to this modality and it is extensible to other imaging systems, such as Delayed Enhancement Computed Tomography.

As in [20], [24], the Laplace equation is employed to provide a harmonic function between the endocardium and the epicardium, whose streamlines yield a point-to-point correspondence between both surfaces but, unlike [20], these streamlines do not need to be explicitly computed and only the harmonic function is necessary. This allows for the interpretation of transmurality as a dense scalar field, as well as to visualize it as a 3D rendering. Transmurality

mapping and visualization has been studied in [26], although its computation was performed slice-by-slice by a 2D method based on [11], with 100 sectors per slice. Significant variations of the transmurality using different spatial resolutions were also reported. Using the proposed methodology it is possible to extract a map of the fully 3D subendocardial local transmurality at any depth of the myocardium. This makes our maps of potential help in intra cavity ablation contexts, since the scar present at the subendocardial half-wall of the myocardium correlates better with endocardial electroanatomic voltage maps [18] than the scar in the whole myocardium.

This paper is organized as follows. Section II gives a brief description of the most closely related Fast Marching (FM) methods to the one proposed here. The MSSFM method differential formulation and numerical scheme are described in Sections III-A and III-B respectively. The computation of the transmurality maps is detailed in Section IV. In Section V, experiments performed on both synthetic and real images are described and Section VI gathers conclusions of this work.

II. Related Work

A. Yezzi's Approach to Thickness Computation

Transmurality computation relies on the ability of measuring thickness. In the context of neurology, cortical thickness measurement has been an active field of research due to the difficulties that the convoluted geometry of gray matter poses. A brief overview on the problem is given in [23], [24].

In [24], Yezzi and Prince proposed a PDE framework to compute thickness at any point $\mathbf{x}$ as it was defined in [23], that is, the total arclength of a unique curve (or correspondence trajectory) passing through $\mathbf{x}$ connecting an inner Γ_0 and an outer Γ_1 boundaries of an image region $R \subset \mathbb{R}^N, N = 2, 3$. Γ_0 and Γ_1 must be simply connected, and R must have exactly these two boundaries [23]. Note that with this definition, all the points in the correspondence trajectory have the same thickness. Therefore, a family of non-intersecting curves providing a bijection between the boundaries is needed.

The thickness is computed as $W(\mathbf{x}) = T(\mathbf{x}) + \tilde{T}(\mathbf{x})$, where $T(\mathbf{x})$ and $\tilde{T}(\mathbf{x})$ are the solution of the following PDEs with boundary conditions:

$$\mathbf{V}(\mathbf{x}) \cdot \nabla T(\mathbf{x}) = 1, \text{ subject to } T(\Gamma_0) = 0 \tag{1}$$

$$-\mathbf{V}(\mathbf{x}) \cdot \nabla \tilde{T}(\mathbf{x}) = 1, \text{ subject to } \tilde{T}(\Gamma_1) = 0 \tag{2}$$

where $\mathbf{V}(\mathbf{x})$ is a unitary vector field tangent to the correspondence trajectories. Two choices are a normalized gradient vector flow field [27] and the normalized gradient of a harmonic function that solves Laplace's equation in R, with boundary conditions on Γ_0 and Γ_1 [24]. The solution of Eqs. (1) and (2) is given by first-order upwind numerical schemes (see [24] for details).

This thickness computation framework [24] was not designed to compute non-viable tissue transmurality, and it is not straightforwardly adaptable to that end due to the following reasons. Myocardial scar may have an arbitrary topology, often appearing as islands within the myocardium, and therefore two unconnected boundaries may not appear in general, which would invalidate the premises established in [24]. Even the division of the scar perimeter

into artificial boundaries would pose further difficulties. Since the same vector field $\mathbf{V}(\mathbf{x})$ should be used to compute both the myocardial and the scar thickness, a previous analysis would need to be done to partition the damaged tissue into connected regions where no myocardial correspondence trajectory crossed healthy tissue. The explicit computation of these trajectories should then be forcibly carried out, which [24] tried to avoid. These problems stem from the fact that Eqs. (1) and (2) consider that the cost of moving from one point to another depends exclusively on the direction given by $\mathbf{V}(\mathbf{x})$.

B. The Fast Marching Method

This method, proposed in [28] as a front propagation algorithm, allows the assignment of scalar costs to every node by means of a propagation speed. Let $\Omega \subset \mathbb{R}^N$, and let $\Gamma(t)$ be a monotonically advancing front in Ω, whose speed component in the normal direction is $F(\mathbf{x})$. The original Fast Marching method [28] computes the arrival times $T(\mathbf{x})$ of the front to any point $\mathbf{x}=(x_1,\ldots,x_N)\in\Omega$, by solving the boundary value problem:

$$\begin{aligned} |\nabla T(\mathbf{x})|F(\mathbf{x}) &= 1, \\ T(\Gamma(0)) &= 0 \end{aligned} \tag{3}$$

with $F(\mathbf{x})>0$. For $F(\mathbf{x})=1$, $T(\mathbf{x})$ yields an approximation of the Euclidean distance to $\Gamma(0)$. The proposed algorithm is based on an upwind finite differences numerical scheme to update node values, and it is solved in one pass by always freezing the node with the lowest $T(\mathbf{x})$ value and updating its neighbors. Further details of the Fast Marching numerical implementation may be found in [28]–[30].

The Fast Marching method is not in general suitable to compute thickness or transmurality, however, because the propagation of the front may follow any arbitrary direction in Ω.

To illustrate this, let us consider how the myocardial and scar thickness could be approximated with Euclidean distances by creating two maps defined over the myocardium, $D_m(\mathbf{x})$ and $D_s(\mathbf{x})$:

1. $D_m(\mathbf{x})$ is the Euclidean distance from the point $\mathbf{x}$ to the endocardium, which will be computed with the Fast Marching method with the endocardium as $\Gamma(0)$ and moving at a uniform speed $F_m(\mathbf{x})=1$.
2. $D_s(\mathbf{x})$ is the outcome of the Fast Marching method, which starts its propagation from the endocardium with speed $F_s(\mathbf{x})=\exp(8\chi_s(\mathbf{x}))$. The propagation speed depends on whether $\mathbf{x}$ is located or not within the scar provided by the indicator function $\chi_s(\mathbf{x})$. It is used to approximate the scar thickness as $D_m(\mathbf{x})-D_s(\mathbf{x})$.

Let us now create a map $t_E(\mathbf{x})$ where any point $\mathbf{x}$ of the myocardium is associated with the fraction of the Euclidean distance from that point to the endocardium that was covered by non-viable tissue.

$$t_E(\mathbf{x}) = \frac{D_m(\mathbf{x}) - D_s(\mathbf{x})}{D_m(\mathbf{x})} \tag{4}$$

The value of $t_E(\mathbf{x})$ at the epicardium would be the scar transmurality, defined as the ratio of non-viable tissue within the myocardial thickness; but at middle points, this map would change differently for different scar configurations even if they had the same amount of non-viable tissue.

In Figure 2(a) we show a segmented slice of a myocardium with a scar. The healthy and scarred myocardial tissues are given in black and white respectively and the background is colored in gray. Figures 2(b), 2(c) and 2(d) show the computed $t_E(\mathbf{x})$, $D_m(\mathbf{x})$ and $D_m(\mathbf{x})-D_s(\mathbf{x})$ maps respectively.

There is a region (pointed to by the white arrow) in Figure 2(a) where the myocardium is occupied by both scar and healthy tissue. The transmurality in that region should thus have intermediate values; however, Figure 2(b) shows that $t_E(\mathbf{x}) = 1$ at the epicardium. This would mean that the whole myocardial thickness is fully composed of damaged tissue, which clearly is not the case. Moreover, at some neighboring epicardium (on the right of the annotated radius, pointed by the black arrow) where no scar is present, $t_E(\mathbf{x})$ takes on values different from zero, the expected transmurality value at those points.

The reason for these disagreements lies in the maps $D_m(\mathbf{x})$ and $D_m(\mathbf{x})-D_s(\mathbf{x})$ (Figures 2(c) and 2(d) respectively). While $D_m(\mathbf{x})$ shows the expected behavior of a myocardial thickness map, $D_m(\mathbf{x})-D_s(\mathbf{x})$ takes on higher values than expected at the regions pointed by the white and black arrows. This is due to the fact that the Fast Marching method assumes that, unlike [24], the propagating front may evolve unrestricted by direction. Accordingly, nodes with low $D_s(\mathbf{x})$ values influence all their neighbors regardless of the endocardial-epicardial direction, causing a leaking that may be appraised in Figure 2(d). Consequently, a front-propagation method to compute distances only along a meaningful direction would be needed to overcome these limitations in the computation of thickness and transmurality with an Eulerian framework.

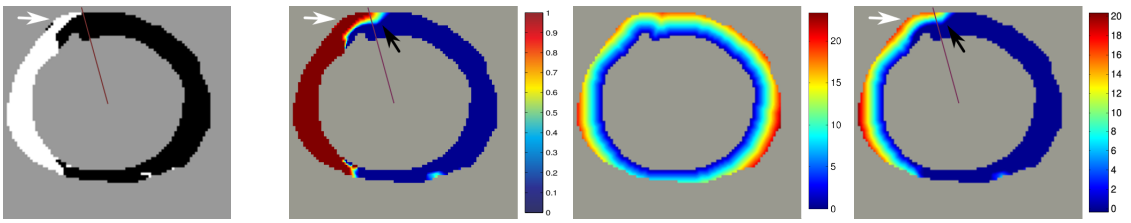

(a) (b) (c) (d)

Figure 2. (a) Scar segmentation $\chi_s(\mathbf{x})$ that produces the following maps with the Fast Marching method: (b) transmurality $t_E(\mathbf{x})$, (c) myocardial thickness $D_m(\mathbf{x})$, and (d) scar thickness $D_m(\mathbf{x})-D_s(\mathbf{x})$.

III. Multi-Stencil Streamline Fast Marching Method

A. Differential Formulation

Let $R \subset \Omega \subset \mathbb{R}^N$ be a spatial region, let Γ_0, Γ_1 be two non-intersecting, simply connected hypersurfaces contained in the boundary of R, and let $s(\mathbf{x})$ be a function that satisfies the following properties:

1) It is defined in $\Gamma_0 \cup R \cup \Gamma_1$ and differentiable in R.
2) The streamlines of $s(\mathbf{x})$ cannot cross each other in $\Gamma_0 \cup R \cup \Gamma_1$.
3) For every point in $\Gamma_0 \cup R \cup \Gamma_1$, there is a single streamline passing through which connects Γ_0 with Γ_1.
4) The values of $s(\mathbf{x})$ when moving along any streamline from Γ_0 to Γ_1 are monotonically increasing.

To include a directional restriction in Eq. (3), we redefine $T(\mathbf{x})$ to be the arrival time to the point $\mathbf{x} \in R$ of a particle moving with speed $F(\mathbf{x})$ along the streamline of $s(\mathbf{x})$ passing through, whose initial position was in Γ_0. To do this, we propose to solve the 1D Eikonal equation:

$$|D_{\nabla s} T(\mathbf{x})| F(\mathbf{x}) = 1, \text{ subject to } T(\Gamma_0) = 0 \tag{5}$$

where $D_{\nabla s} T$ is the directional derivative of T in the direction of ∇s, and $F(\mathbf{x}) > 0$ is the speed with which the front moves at $\mathbf{x}$. $D_{\mathbf{v}} T$ can be expressed in terms of ∇T by:

$$D_{\mathbf{v}} T = \frac{\mathbf{v}}{|\mathbf{v}|} \nabla T, \tag{6}$$

which allows Eq. (5) to be reformulated as:

$$\left| \frac{\nabla s(\mathbf{x})}{|\nabla s(\mathbf{x})|} \cdot \nabla T(\mathbf{x}) \right| = C(\mathbf{x}), \text{ subject to } T(\Gamma_0) = 0 \tag{7}$$

where $C(\mathbf{x}) = \frac{1}{F(\mathbf{x})}$ is a different way of representing the cost of a node $\mathbf{x}$ in the computation of $T(\mathbf{x})$ as a local time contribution to the global arrival time $T(\mathbf{x})$.

Then, by means of Eq. (7), the 1D Eikonal equation given by Eq. (5) is solved in $\mathbb{R}^N$ for a family of streamlines given by $s(\mathbf{x})$ simultaneously, as in [24]. In addition, the front propagation is controlled by $C(\mathbf{x})$, which allows for different behaviors on healthy and non-viable myocardial tissue (like [28]) and is thus suitable for computing scar and myocardial thickness.

This method generalizes[1] the thickness computation framework in Section II-A, whose PDEs are given in Eqs. (1) and (2). If we set $C(\mathbf{x}) = 1$, and choose $\mathbf{V}(\mathbf{x}) = \frac{\nabla s(\mathbf{x})}{|\nabla s(\mathbf{x})|}$, Eq. (7) becomes:

$$|\mathbf{V}(\mathbf{x}) \cdot \nabla T(\mathbf{x})| = 1 \tag{8}$$

Taking into account that $s(\mathbf{x})$ is monotonically increasing from Γ_0 to Γ_1 and $T(\mathbf{x})$ is not decreasing along every streamline in R,

$$\mathbf{V}(\mathbf{x}) \cdot \nabla T(\mathbf{x}) = 1 \tag{9}$$

is the correct choice for evolving $T(\mathbf{x})$ from Γ_0 to Γ_1, and is equivalent to Eq. (1). Remark that $-s(\mathbf{x})$ is monotonically increasing from Γ_1 to Γ_0. Then, Eq. (8) translates into:

$$-\mathbf{V}(\mathbf{x}) \cdot \nabla T(\mathbf{x}) = 1 \tag{10}$$

if Γ_0 and Γ_1 are swapped to be respectively the end and start of the propagating front. Thus, Eq. (2) may also be issued from Eq. (7).

For the purpose of computing thickness, we are interested in solving Eq. (7) from Γ_0 to Γ_1 or from Γ_1 to Γ_0 so we can use in both cases a numerical scheme for the upwind equation:

$$\frac{\nabla s(\mathbf{x})}{|\nabla s(\mathbf{x})|} \cdot \nabla T(\mathbf{x}) = C(\mathbf{x}) \tag{11}$$

replacing $s(\mathbf{x})$ by $-s(\mathbf{x})$ if the front is chosen to propagate from Γ_1 instead of from Γ_0.

[1]This method is also a generalization of our preliminary work [31] (where a Radial Fast Marching method for $\mathbb{R}^2$ was proposed) by choosing $s(\mathbf{x})$ to be $s(x, y) = \sqrt{x^2 + y^2}$.

B. Multi-Stencil Numerical scheme

The following numerical scheme stems from the Multistencil Fast Marching method [30], originally proposed for solving Eq. (3), which has the advantage of taking into account the information provided by all the neighboring nodes in order to reduce the numerical error along the diagonal directions. This is achieved by considering derivatives not only along the natural coordinates of the grid, but also in diagonal directions.

Let us define a set of Q stencils $\{\mathcal{S}_i\}_{i=1}^{Q}$, where $\mathcal{S}_i = \{\vec{\mathbf{v}}_j^i\}_{j=1}^{N}$ is a set of N vectors that constitute a basis of $\mathbb{R}^N$. $\vec{\mathbf{v}}_j^i$ is the j-th vector of the i-th stencil. Each of these vectors provides the means to access the immediate nodes of the grid in the discrete domain, along the direction defined by that vector. An example for $\mathbb{R}^2$ is given in Figure 3(a), where the nodes and the vectors of each stencil are shown. If h_κ is the grid spacing along the κ-th dimension, their expressions are $\mathcal{S}_1 = \{\vec{\mathbf{v}}_1^1 = (h_1, 0), \vec{\mathbf{v}}_2^1 = (0, h_2)\}$ for the stencil along the natural coordinates, and $\mathcal{S}_2 = \{\vec{\mathbf{v}}_1^2 = (h_1, h_2), \vec{\mathbf{v}}_2^2 = (-h_1, h_2)\}$ for the stencil that uses the nodes in the diagonals. There are different alternatives of number of stencils Q and their composition in $\mathbb{R}^3$. Following [30], the chosen stencil vectors for $\mathbb{R}^3$, assuming a voxel size of $h_1 \times h_2 \times h_3$, are given in Table II. Note that $\mathcal{S}_1$ covers a 6-neighborhood, $\mathcal{S}_1$–$\mathcal{S}_4$ an 18-neighborhood, and $\mathcal{S}_1$–$\mathcal{S}_6$ a 26-neighborhood.

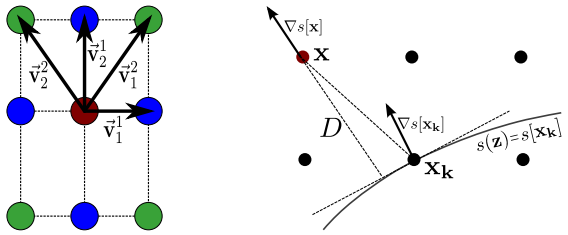

(a) (b)

Figure 3. (a) Description of the stencils used in $\mathbb{R}^2$. (b) 2D graph of the default value computation for $T[\mathbf{x}]$.

Table II
VECTORS THAT COMPOSE THE STENCILS $\mathcal{S}_i$ IN $\mathbb{R}^3$.

$\mathcal{S}_i$	$\vec{\mathbf{v}}_1^i$	$\vec{\mathbf{v}}_2^i$	$\vec{\mathbf{v}}_3^i$
$\mathcal{S}_1$	$(h_1, 0, 0)$	$(0, h_2, 0)$	$(0, 0, h_3)$
$\mathcal{S}_2$	$(h_1, 0, 0)$	$(0, h_2, -h_3)$	$(0, h_2, h_3)$
$\mathcal{S}_3$	$(h_1, 0, -h_3)$	$(0, h_2, 0)$	$(h_1, 0, h_3)$
$\mathcal{S}_4$	$(h_1, h_2, 0)$	$(-h_1, h_2, 0)$	$(0, 0, h_3)$
$\mathcal{S}_5$	$(h_1, 0, h_3)$	$(-h_1, h_2, h_3)$	$(h_1, h_2, -h_3)$
$\mathcal{S}_6$	$(h_1, 0, -h_3)$	(h_1, h_2, h_3)	$(-h_1, h_2, -h_3)$

Let $\mathbf{U}^i = (U_1^i, \ldots, U_N^i)^T$, with $U_j^i = D_{\vec{\mathbf{v}}_j^i} T(\mathbf{x})$ be the vector of directional derivatives of $T(\mathbf{x})$ along the vectors in $\mathcal{S}_i$. As stated in [30], a linear system can be built using Eq. (6) to express $\mathbf{U}^i$ in terms of ∇T:

$$\mathbf{U}^i = R^i \cdot \nabla T, \text{ with } R_{jk}^i = \frac{\mathbf{v}_{jk}^i}{|\vec{\mathbf{v}}_j^i|} \tag{12}$$

Then, Eq. (11) can be reformulated for each stencil as:

$$\frac{\nabla s(\mathbf{x})}{|\nabla s(\mathbf{x})|} \cdot (R^i)^{-1} \cdot \mathbf{U}^i(\mathbf{x}) = C(\mathbf{x}) \tag{13}$$

If $\vec{\alpha}^i := (\alpha_1^i, \ldots, \alpha_N^i) = \frac{\nabla s(\mathbf{x})}{|\nabla s(\mathbf{x})|} \cdot (R^i)^{-1}$, then the equation

$$\sum_{j=1}^{N} \alpha_j^i(\mathbf{x}) U_j^i(\mathbf{x}) = C(\mathbf{x}) \tag{14}$$

must be solved for every $\mathcal{S}_i, i = 1, \ldots, Q$. The directional derivatives in $\mathbf{U}^i$ are approximated by the following forward and backward difference schemes:

$$D^{+\vec{\mathbf{v}}_j^i} T[\mathbf{x}] = \frac{T[\mathbf{x} + \vec{\mathbf{v}}_j^i] - T[\mathbf{x}]}{|\vec{\mathbf{v}}_j^i|} \tag{15}$$

$$D^{-\vec{\mathbf{v}}_j^i} T[\mathbf{x}] = \frac{T[\mathbf{x}] - T[\mathbf{x} - \vec{\mathbf{v}}_j^i]}{|\vec{\mathbf{v}}_j^i|} \tag{16}$$

where the notation $[\cdot]$ means we are in the discrete domain.

As it is also the case of the original Fast Marching method [28], the front propagation direction must be taken into account in the computation of $T[\mathbf{x}]$. Therefore, an upwind finite difference scheme is employed for the numerical scheme. Equation (14) can then be discretized as:

$$\begin{aligned} \sum_{j=1}^{N} \big(& \max(\alpha_j^i[\mathbf{x}], 0) \cdot D^{-\vec{\mathbf{v}}_j^i} T[\mathbf{x}] \\ & + \min(\alpha_j^i[\mathbf{x}], 0) \cdot D^{+\vec{\mathbf{v}}_j^i} T[\mathbf{x}] \big) = C[\mathbf{x}] \end{aligned} \tag{17}$$

which may be expressed as a first order polynomial $\lambda_1^i T[\mathbf{x}] + \lambda_0^i = C[\mathbf{x}]$, where λ_0^i and λ_1^i have the expressions:

$$\lambda_0^i = \sum_{j=1}^{N} \frac{\min(\alpha_j^i[\mathbf{x}], 0) T[\mathbf{x} + \vec{\mathbf{v}}_j^i] - \max(\alpha_j^i[\mathbf{x}], 0) T[\mathbf{x} - \vec{\mathbf{v}}_j^i]}{|\vec{\mathbf{v}}_j^i|} \tag{18}$$

$$\lambda_1^i = \sum_{j=1}^{N} \frac{|\alpha_j^i[\mathbf{x}]|}{|\vec{\mathbf{v}}_j^i|} \tag{19}$$

Then, at each node, a candidate value $T^i[\mathbf{x}]$ can be computed for every stencil as:

$$T^i[\mathbf{x}] = \frac{C[\mathbf{x}] - \lambda_0^i}{\lambda_1^i} \tag{20}$$

We must check that the computed $T^i[\mathbf{x}], i = 1, \ldots, Q$ satisfy the causality condition, that is, that their value is larger than the rest of the arrival times already known in the streamline. For this, the value of a known[2] node $\mathbf{x}_k$, $T[\mathbf{x}_k]$, will be used to reject those candidates for which $T^i[\mathbf{x}] < T[\mathbf{x}_k]$ is true. The node $\mathbf{x}_k$ is chosen as:

$$\mathbf{x}_k = \arg\max_{\mathbf{x}_c} \left(\frac{s[\mathbf{x}] - s[\mathbf{x}_c]}{|\mathbf{x} - \mathbf{x}_c|} \right) \tag{21}$$

where $\mathbf{x}_c$ are the locations of those nodes in the neighborhood with known values. Then, $T[\mathbf{x}]$ is chosen as the minimum $T^i[\mathbf{x}]$ that satisfies the causality condition $T^i[\mathbf{x}] \geq T[\mathbf{x}_k]$. If no $T^i[\mathbf{x}]$ meets it, a default value for $T[\mathbf{x}]$

[2]The value of known nodes is fully computed and frozen (see Section IV-A).

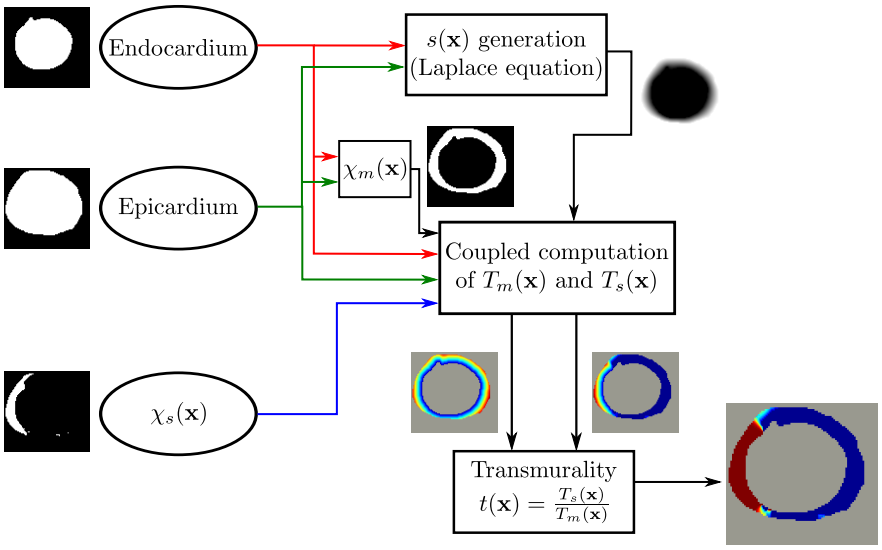

Figure 4. General flowchart of the computation of $t(\mathbf{x})$.

is computed as $T[\mathbf{x}] = T[\mathbf{x}_k] + C[\mathbf{x}] \cdot D$, where D is the length of the segment between $\mathbf{x}$ and the isocontour $\{\mathbf{z} : s(\mathbf{z}) = s[\mathbf{x}_k]\}$ along the direction given by $\nabla s[\mathbf{x}]$. If the isocontour is approximated by its tangent plane in $\mathbf{x}_k$, D can be approximated by trigonometry. Figure 3(b) contains a graph of the elements that take part in the computation of the default value.

IV. Transmurality Maps

A. Definition and Calculation

Our goal is to define transmurality as a function whose domain is the myocardium, which not only provides the transmurality values that the existing 2D methods offer, but also supplies information about the scar depth location. In addition, it is computed as a fully 3D method. We assume that segmentations of the endocardium, the epicardium and the scar are available. A general flowchart of the proposed framework for the computation of transmurality maps is drawn in Figure 4, using the same inputs as in Figure 2. Note how the proposed framework overcomes the limitations of the FM method to compute transmurality.

The first step is to have an appropriate $s(\mathbf{x})$ for each particular myocardium, since there is a high variability in their geometry. The following Laplace equation with boundary conditions is solved within the myocardium:

$$\nabla^2 s(\mathbf{x}) = 0, \text{ subject to } s(\Gamma_0) = 0, s(\Gamma_1) = 1 \tag{22}$$

with Γ_0 and Γ_1 being respectively the endocardial and the epicardial boundaries. The harmonic function $s(\mathbf{x})$ that solves Eq. (22) satisfies the properties given in Section III-A, and also provides a unique point-to-point mapping between Γ_0 and Γ_1 [23]. Nevertheless, if the transmurality map methodology were to be applied in a different context (for example, in a setting where the object geometry was fixed and known beforehand), a different choice

for $s(\mathbf{x})$ might be considered without loss of generality as long as the aforementioned properties were satisfied. Figure 5 shows some streamlines, in 3D and projected on an SA and an LA plane, computed out of the harmonic function $s(\mathbf{x})$ yielded by solving Laplace's equation in a real CE-CMR dataset.

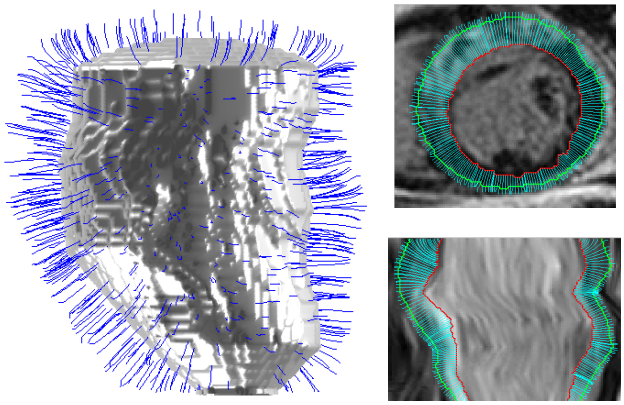

Figure 5. Left: 3D rendering of some streamlines from a harmonic function $s(\mathbf{x})$, computed from a real dataset, superposed to the endocardial surface. Right: projection of the streamlines on an SA plane (top) and an LA plane (bottom).

In the next step $T_s(\mathbf{x})$ and $T_m(\mathbf{x})$, respectively the scar and myocardial thickness maps, are simultaneously computed by means of the MSSFM method with the same harmonic function $s(\mathbf{x})$ and different local costs $C_s(\mathbf{x})$ and $C_m(\mathbf{x})$. Let $\chi_s(\mathbf{x})$ and $\chi_m(\mathbf{x})$ be the characteristic functions of the scar and the myocardium segmentations respectively, such that $\chi_\nu \in [0,1], \nu = s,m$, with the extreme situations of $\chi_\nu = 1$ if $\mathbf{x}$ is within the tissue of interest (scar or myocardium) and $\chi_\nu = 0$ otherwise. Note that $\chi_\nu(\mathbf{x})$ does not need to only take on the binary values $\{0,1\}$, a fact that opens up possibilities such as taking into account the existence of tissue mixtures inside a voxel and soft segmentations. Then, to compute the scar and myocardial thickness, the local costs are chosen to be $C_s(\mathbf{x}) = \chi_s(\mathbf{x})$ and $C_m(\mathbf{x}) = \chi_m(\mathbf{x})$. The following algorithm computes $T_s[\mathbf{x}]$ and $T_m[\mathbf{x}]$ simultaneously[3]:

1. Label all the nodes enclosed by the endocardium as *Known*, and set their value $T_s[\mathbf{x}] = T_m[\mathbf{x}] = 0$. Label the remaining nodes as *Far*.
2. Build a narrow band with the *Far* neighbors of *Known* nodes, label them as *Active*, compute $T_s[\mathbf{x}]$ and $T_m[\mathbf{x}]$ (see Section III-B), and add them to the heap.
3. While there are *Active* nodes within the myocardium:
   a Find the *Active* node with the smallest $s[\mathbf{x}]$ value, and mark it as *Known*.
   b Look for its neighbors within the myocardium whose label is not *Known*. Change those with a *Far* label to *Active* and add them to the heap. Compute $T_s[\mathbf{x}]$ and $T_m[\mathbf{x}]$ (see Section III-B).
   c Go back to step 3.

[3]We change from the continuous domain $(\mathbf{x})$ to the discrete domain $[\mathbf{x}]$ to match the notation in Section III-B. The continuous notation is resumed afterwards.

In steps 2 and 3.b, after computing $T_s^i[\mathbf{x}]$ and $T_m^i[\mathbf{x}]$ for every stencil $\mathcal{S}_i, i = 1, \ldots, Q$, we assign $T_s[\mathbf{x}] = T_s^j[\mathbf{x}]$ and $T_m[\mathbf{x}] = T_m^j[\mathbf{x}]$ from the stencil $\mathcal{S}_j$ with the smallest value of $T_m^i[\mathbf{x}]$. If in the computation of either $T_s(\mathbf{x})$ or $T_m(\mathbf{x})$ a default value from the causality condition needs to be used, then default values must be computed for both $T_s(\mathbf{x})$ and $T_m(\mathbf{x})$. This is done because as long as the same stencil is used for computing $T_s[\mathbf{x}]$ and $T_m[\mathbf{x}]$, and $C_s[\mathbf{x}] \leq C_m[\mathbf{x}], \forall \mathbf{x} \in R$, then $T_s[\mathbf{x}] \leq T_m[\mathbf{x}], \forall \mathbf{x} \in R$ which ensures that the computed transmurality will only take on values in $[0, 1]$.

Finally, the transmurality map $t(\mathbf{x})$ is computed as:

$$t(\mathbf{x}) = \frac{T_s(\mathbf{x})}{T_m(\mathbf{x})} \tag{23}$$

Within the myocardium, $t(\mathbf{x})$ is the transmurality using the piece of streamline between $\mathbf{x}$ and the endocardium. At the epicardial nodes, $t(\mathbf{x})$ provides the transmurality using the whole myocardial thickness in the same manner as state-of-the-art transmurality methods do. Therefore, at the rest of the myocardium $t(\mathbf{x})$ supplies additional information over the intramural location of the damaged tissue.

For visualization purposes, however, it may be convenient to assign the same transmurality value to all the points in a streamline, as it is done in [24]. This can be easily performed by computing $\tilde{T}_s(\mathbf{x})$ and $\tilde{T}_m(\mathbf{x})$ using $\tilde{C}_s(\mathbf{x}) = C_s(\mathbf{x})$ and $\tilde{C}_m(\mathbf{x}) = C_m(\mathbf{x})$ respectively, but employing $\tilde{s}(\mathbf{x}) = -s(\mathbf{x})$ and swapping the contours (using the epicardium as $\tilde{\Gamma}_0$ and the endocardium as $\tilde{\Gamma}_1$). The expression for the transmurality when all the points in a streamline have the same value, $\hat{t}(\mathbf{x})$, is:

$$\hat{t}(\mathbf{x}) = \frac{T_s(\mathbf{x}) + \tilde{T}_s(\mathbf{x})}{T_m(\mathbf{x}) + \tilde{T}_m(\mathbf{x})} \tag{24}$$

In order to provide better accuracy to the MSSFM method, upsampled segmentations may be used to compute $T_s(\mathbf{x})$ and $T_m(\mathbf{x})$, and then return to the original resolution by decimation.

B. Visualization of 3D Local Transmurality Maps

The inspection of a myocardial 3D local transmurality map poses a challenge, since depth adds further complexity to the visualization on top of the 3D myocardial geometry and the transmurality value. One of the possibilities is to use 3D rendering techniques; for example, to employ an isosurface of $s(\mathbf{x})$ at a certain depth value and encode the transmurality as the isosurface color. This approach allows for a good representation of the myocardial shape, but only one isosurface is shown at a time, and always some part of the myocardium is hidden to the viewer.

A different possibility is to use a 3D to 2D map projection that allows for the visualization of the whole isosurface, in the same manner the Earth surface is depicted on a cartographic plane. As a result there are no occlusions in the visualization, and several 2D maps at different depths can be observed simultaneously.

Let $\{\Psi : 0 \leq v \leq v_{\max} \leq \frac{\pi}{2}, -\pi \cos v \leq u \leq \pi \cos v\}$ be the 2D domain in which the isosurface $s(x, y, z) = s_0$ is to be mapped, let the ventricle long axis be roughly aligned with the z-axis, and let (u, v) be a point in Ψ. The z coordinate is mapped onto v, such that $v = 0$ and $v = \frac{\pi}{2}$ belong to the ventricle basis and apex, respectively. If the apex is not present in the volume, a value $v_{\max} \leq \frac{\pi}{2}$ is computed as $v_{\max} = \arctan\left(\frac{\Delta z}{\Delta r}\right)$, where Δz is the

ventricle length in the z-axis and Δr the ventricle radius of the most apical short-axis slice. Then, to extract the isosurface point that maps into (u, v), a ray is traced along the following coordinates:

$$\begin{aligned} x &= x_0(v) + r\cos\left(\frac{u}{\cos v} + \theta_0\right) \\ y &= y_0(v) + r\sin\left(\frac{u}{\cos v} + \theta_0\right) \\ z &= z_0 + z_{\max}\frac{v}{v_{\max}} \end{aligned} \tag{25}$$

where $r \geq 0$ controls the location of the isosurface within the myocardium thickness, $(x_0(v), y_0(v))$ are the coordinates of the ventricle long axis, θ_0 is an angular offset to allow for a rotation of the ray around the ventricle long axis (see Section V-C3), and z_0 and $z_{\max}$ are the z coordinates of the most basal and apical myocardial slices. The value assigned to (u, v) is the value of the transmurality local map where this ray crosses the isosurface of $s(\mathbf{x})$ at the desired depth.

V. Experimental Results

The experimentation is divided into three parts. The accuracy and consistency of the Streamline Fast Marching is tested in Section V-A. Then, a comparison between the proposed and existing 2D methods for transmurality computation is carried out using a 3D synthetic model in Section V-B. Finally, in Section V-C the transmurality maps of real datasets are shown and their capability to distinguish different scar configurations is discussed.

A. Accuracy and Consistency of the MSSFM

1) Experimental Design: Following the methodology of [30], a number of analytical functions $T_i(\mathbf{x})$, $s_i(\mathbf{x})$ and $C_i(\mathbf{x})$ that together satisfy Eq. (7) are employed as the gold standard to compare the computed $T_i[\mathbf{x}]$. These analytical functions are given in Table III; the first four are 2D and the remaining three are 3D. Given that $T_1(\mathbf{x})$ and $T_5(\mathbf{x})$ have unitary speed, their computational outcome can be compared with the result provided by the upwind PDE for thickness computation (given by Eq. (1)) proposed in [24]. In Figures 6(a)–6(d), the isocontours of the 2D analytical functions $T_i(\mathbf{x}), i = 1, \ldots, 4$ are drawn.

The error committed by the numerical scheme is measured by means of the L_1 and L_∞ norms of the absolute difference between the computed $T_i[\mathbf{x}]$ and the analytical $T_i(\mathbf{x})$:

$$L_1^i = \frac{\sum_{j=1}^{N} |T_i[\mathbf{x}_j] - T_i(\mathbf{x}_j)|}{N} \tag{26}$$

$$L_\infty^i = \max_{j=1,\ldots,N} \left(|T_i[\mathbf{x}_j] - T_i(\mathbf{x}_j)|\right) \tag{27}$$

where N is the number of nodes in the discretized domain. We also employ a normalized version of these norms, $L_{1n}^i = \frac{L_1^i}{\max(T_i)}$ and $L_{\infty n}^i = \frac{L_\infty^i}{\max(T_i)}$, to account for the variations in range of the different T_i.

Table III

ANALYTICAL FUNCTIONS EMPLOYED IN THE EXPERIMENTS.

i	$T_i(\mathbf{x})$	$s_i(\mathbf{x})$	$C_i(\mathbf{x})$
1	$\sqrt{x^2+y^2}$	$\sqrt{x^2+y^2}$	1
2	$\sqrt{x^2+y^2}-2\sin\left(\frac{\sqrt{x^2+y^2}}{2}\right)$	$\sqrt{x^2+y^2}$	$1-\cos\left(\frac{\sqrt{x^2+y^2}}{2}\right)$
3	$\frac{x^2}{25}+\frac{y^2}{9}$	$\sqrt{x^2+y^2}$	$\frac{18x^2+50y^2}{225\sqrt{x^2+y^2}}$
4	$\frac{x^2}{100}+\frac{y^2}{20}$	$\sqrt{x^2+y^2}$	$\frac{x^2+5y^2}{50\sqrt{x^2+y^2}}$
5	$\sqrt{x^2+y^2+z^2}$	$\sqrt{x^2+y^2+z^2}$	1
6	$\sqrt{x^2+y^2+z^2}-3\sin\left(\frac{\sqrt{x^2+y^2+z^2}}{3}\right)$	$\sqrt{x^2+y^2+z^2}$	$1-\cos\left(\frac{\sqrt{x^2+y^2+z^2}}{3}\right)$
7	$\frac{x^2}{50}+\frac{y^2}{20}+\frac{z^2}{100}$	$\sqrt{x^2+y^2+z^2}$	$\frac{2x^2+5y^2+z^2}{50\sqrt{x^2+y^2+z^2}}$

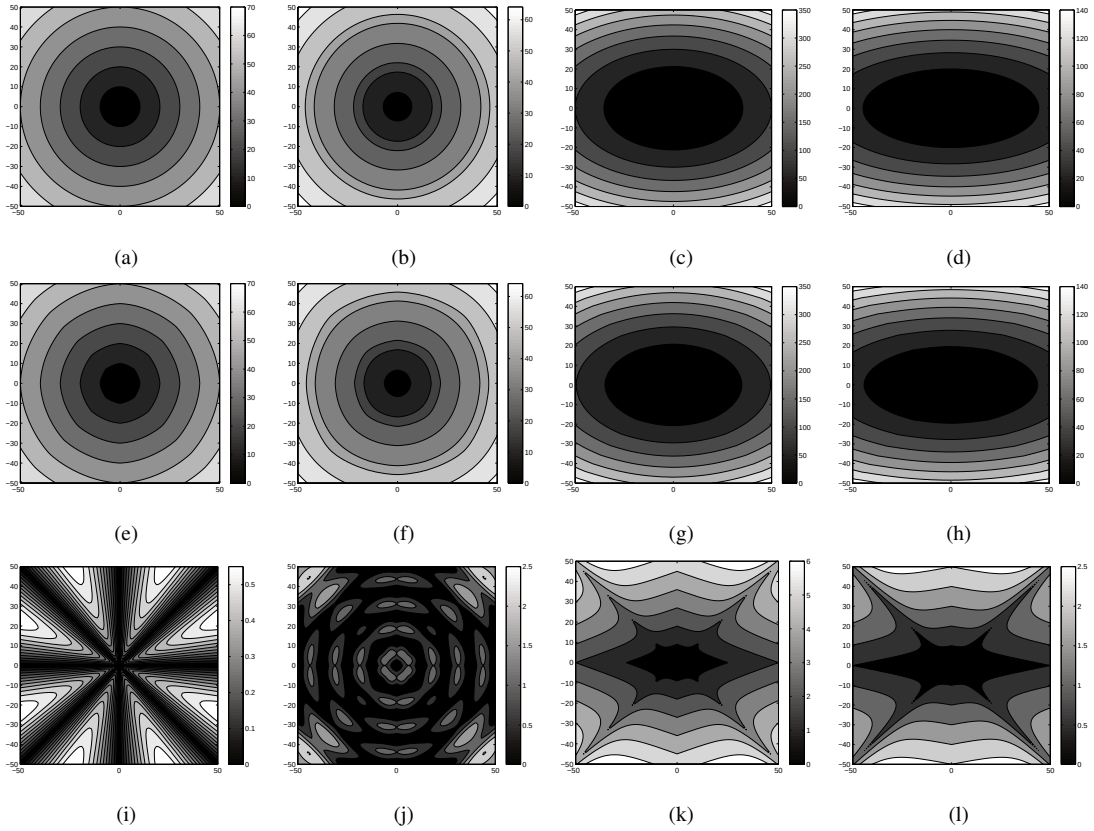

(a) (b) (c) (d)

(e) (f) (g) (h)

(i) (j) (k) (l)

Figure 6. Results for $T_1(\mathbf{x})$, with isotropic grid spacing $h = 1$. (a)–(d): Analytical functions $T_i(\mathbf{x}), i = 1,\ldots,4$. (e)–(h): Computed $T_i[\mathbf{x}], i = 1,\ldots,4$. (i)–(l): Absolute error $|T_i(\mathbf{x}) - T_i[\mathbf{x}]|, i = 1,\ldots,4$.

2) Accuracy: In Figures 6(e)–6(h), the computed $T_i[\mathbf{x}], i = 1,\ldots,4$ are also shown as isocontours, whereas the absolute error with respect to the analytical solution is shown in Figures 6(i)–6(l). In Table IV, the L_1 and L_∞ norms for each $T_i(\mathbf{x})$ computed by the proposed multi-stencil scheme (and when possible, also by the thickness computation method [24]) are given, using $h_1 = h_2 = 1$, $-50 \leq x, y \leq 50$ for the 2D test functions T_1 to T_4 and

Table IV

COMPUTED NORMS BETWEEN THE PROPOSED MULTI-STENCIL METHOD AND THE METHOD [24], WHEN APPLICABLE (T_1 AND T_5).

i	$\max(T_i)$	MSSFM		Method [24]	
		L^i_{1n}	$L^i_{\infty n}$	L^i_{1n}	$L^i_{\infty n}$
1	70.711	4.35×10^{-3}	8.34×10^{-3}	1.12×10^{-2}	1.90×10^{-2}
2	72.142	9.54×10^{-3}	3.48×10^{-2}	—	—
3	377.778	9.19×10^{-3}	1.75×10^{-2}	—	—
4	150.000	8.72×10^{-3}	1.80×10^{-2}	—	—
5	51.961	7.54×10^{-3}	1.48×10^{-2}	2.52×10^{-2}	3.94×10^{-2}
6	54.959	1.16×10^{-2}	2.80×10^{-2}	—	—
7	72.000	1.40×10^{-2}	2.69×10^{-2}	—	—

$h_1 = h_2 = h_3 = 1$, $-30 \leq x, y, z \leq 30$ for the remaining T_5 to T_7. It may be observed that the proposed method yields more accurate results than [24] for $T_1(\mathbf{x})$ and $T_5(\mathbf{x})$, due to the fact that [24] only uses one stencil ($\mathcal{S}_1$) in its numerical scheme. Therefore, the information provided by the rest of the neighboring nodes is not employed, which makes the error grow. It is worth noting that the L_1 norm yielded by [24] surpasses the L_∞ norm yielded by the proposed multi-stencil method. We remark that the accuracy results for $T_4(\mathbf{x})$ are slightly better than the ones achieved for the same function by the original first-order multi-stencil method proposed for solving the Eikonal equation [30] in the same experimental conditions, which scored $L_1 = 1.515$ and $L_\infty = 3.000$, while the MSSFM yielded $L^4_1 = 1.308$ and $L^4_\infty = 2.697$. The error behavior shown in Figures 6(i)–6(l) may be explained studying the error along the stencil directions, where the numerical scheme can be viewed as a 1D numerical integration of $C_i(\mathbf{x})$. In Figure 6(i) it can be seen that for the constant $C_1(\mathbf{x})$ the error along the stencil directions is zero, and it grows as we move away from them. In Figures 6(j) and 6(l) the local costs $C_3(\mathbf{x})$ and $C_4(\mathbf{x})$ are no longer constant but increasing. Since the value computation —see Eq. (20)— assumes the local cost is constant in the neighborhood, an overestimation occurs. Again, the error increases far from the stencil directions. Lastly, Figure 6(k) shows the error for the sinusoidal local cost $C_2(\mathbf{x})$. The observed pattern is originated because the overestimations when $C_2(\mathbf{x})$ increases are subsequently compensated by underestimations when $C_2(\mathbf{x})$ diminishes.

3) Influence of the Stencil Set: In Table V we show a comparison of the method accuracy and computational cost using one, four and six stencils to compute $T_5[\mathbf{x}]$, $T_6[\mathbf{x}]$ and $T_7[\mathbf{x}]$ with the same discretization as before. The computational cost is measured by the execution time of an implementation of the algorithm in C++ on a computer with an Intel Core(TM) i7-2670QM at 2.20GHz CPU and 8GB of RAM. We can see that the accuracy increases with the number of stencils. In particular, except for T_7, the maximum absolute error L^i_∞ achieved by using 6 stencils is less than the mean absolute error L^i_1 that is yielded when 1 stencil is employed. There is, however, a reduction of the execution time by using one and four stencils of a 52% and a 20% respectively compared with using six stencils.

4) Consistency: Another experiment has been performed to check the numerical scheme consistency, i.e., whether the numerical scheme error tends to zero as the grid spacing does. For this purpose, an isotropic grid of pixel size

Table V

ERROR NORMS AND EXECUTION TIME USING DIFFERENT STENCIL SETS TO COMPUTE T_5, T_6 AND T_7.

Exp.	6 stencils			4 stencils			1 stencil		
	L_1^i	L_∞^i	Time	L_1^i	L_∞^i	Time	L_1^i	L_∞^i	Time
T_5	0.392	0.771	51 s	0.688	1.102	40 s	1.322	2.237	24 s
T_6	0.639	1.541	50 s	0.781	1.625	40 s	1.579	2.784	24 s
T_7	1.008	1.936	50 s	1.008	1.936	40 s	1.238	4.026	24 s

Table VI

CONSISTENCY RESULTS FOR T_1 AND T_3 VARYING THE GRID SPACING h.

h	T_1		T_3	
	L_1^i	L_∞^i	L_1^i	L_∞^i
2^{-4}	1.22×10^{-2}	2.36×10^{-2}	4.40×10^{-3}	8.18×10^{-3}
2^{-5}	8.16×10^{-3}	1.57×10^{-2}	2.17×10^{-3}	4.11×10^{-3}
2^{-6}	5.22×10^{-3}	1.00×10^{-2}	1.09×10^{-3}	2.08×10^{-3}
2^{-7}	3.22×10^{-3}	6.18×10^{-3}	5.50×10^{-4}	1.06×10^{-3}
2^{-8}	1.94×10^{-3}	3.71×10^{-3}	2.79×10^{-4}	5.37×10^{-4}

$h \times h$ has been used to generate $T_1[\mathbf{x}]$ and $T_3[\mathbf{x}]$ with different resolutions. In Table VI the computed errors for different h values show that for smaller h the error diminishes, as expected. In contrast with the results in Table IV, the error norm values for $T_3[\mathbf{x}]$ in Table VI are smaller than for $T_1[\mathbf{x}]$. The reason for this is that the grid size and spacing are chosen to discretize the domain $[-1,1] \times [-1,1]$, in which $C_2(\mathbf{x}) \leq C_1(\mathbf{x})$.

B. Validation using a Synthetic Model

1) Model Description: To assess the accuracy of the transmurality measures provided by the existing 2D methods and the proposed 3D algorithm on the left ventricle, a myocardium-like synthetic phantom has been built using semi-ellipsoids for the endocardium and the epicardium. The endocardium is given by:

$$\frac{x^2}{R_x^2} + \frac{y^2}{R_y^2} + \frac{z^2}{R_z^2} = 1, -80 \leq x, y \leq 80, 0 \leq z \leq 80 \tag{28}$$

with $R_x = R_y = 30$, $R_z = 50$, and a resolution of $160 \times 160 \times 80$. The epicardium is built using new semiaxes $\hat{R}_x = R_x + D_x$, $\hat{R}_y = R_y + D_y$ and $\hat{R}_z = R_z + D_z$, where $D_{\{x,y,z\}}$=16 are the thicknesses along each respective axis. The myocardium is then divided into twelve sectors, whose geometry is shown in Figure 7. Instead of using planes perpendicular to the z-axis for the boundaries between basal, mid-cavity and apical sectors, two cones with the z-axis as their axis of revolution were used which intersect the endocardium at $z_{en_1} = 20$ and $z_{en_2} = 40$ (see Figure 7). Their generatrices are parallel to the endocardium normal at the point of intersection, to better emulate the propagation of ischemia from the endocardium to the epicardium. Each sector is given a random scar transmurality

(a) (b) (c)

Figure 7. (a) LA (left) and bull's eye with sector numbers (right) views of the synthetic myocardium used in the experiments. (b) LA view of two instances of the phantom with a pitch angle of 0° (left) and 20° (right) and a null yaw angle, where the scar is colored by sector. (c) Superposition of the endocardial (red) and epicardial (green) contours at z=0 of all the instances with modified radii and thicknesses.

value $t_i \in [0,1], i = 1, \ldots, 12$, and the scar is computed with the expression:

$$\chi_s(x,y,z) = \sum_{i=1}^{12} H\Big\{1 - \Big(\frac{x^2}{(R_x + t_i D_x)^2} + \frac{y^2}{(R_y + t_i D_y)^2} + \frac{z^2}{(R_z + t_i D_z)^2}\Big)^{\frac{1}{2}}, 0.01\Big\}\chi_i(x,y,z) \tag{29}$$

where $\chi_i(x,y,z) \in \{0,1\}$ is the characteristic function of membership to sector i and $H(\cdot,\varepsilon) \in [0,1]$ is a well known regularized Heaviside function whose expression is:

$$H(u,\varepsilon) = \begin{cases} 1, & u > \varepsilon \\ 0, & u < -\varepsilon \\ \frac{1}{2}\left(1 + \frac{u}{\varepsilon} + \frac{1}{\pi}\sin\left(\frac{u\pi}{\varepsilon}\right)\right), & |u| \leq \varepsilon \end{cases} \tag{30}$$

Note that $\chi_s(x,y,z)$ may have non integer values in a small band. The scar has constant transmurality within a sector, but there are abrupt changes in scar thickness at the boundaries between neighboring sectors.

2) Comparison with 2D Transmurality Methods: To compute the transmurality with the 2D methods described in Nazarian et al. [11], Schuijf et al. [19] and Elnakib et al. [20], the myocardium was divided into slices along the z-axis. Given that the sector boundaries are not orthogonal to the z-axis, a ray may be traced along more than one sector. In that case, the computed transmurality is considered to belong to the sector that has the largest number of nodes along the ray. A 3D transmurality map was computed using the proposed method, upsampling the phantom by 2. The experiment was repeated 100 times for different random sector transmurality configurations.

Two error types are defined. ξ_s is defined as the error committed in the estimation of the transmurality in sector s by averaging all its N_s individual transmurality measures $\tilde{t}_s^i$:

$$\xi_s = \left| t_s - \frac{1}{N_s} \sum_{\langle N_s \rangle} \tilde{t}_s^i \right| \tag{31}$$

A local error LE^i is defined as the absolute deviation of an individual transmurality measure $\tilde{t}_{s(i)}^i$ with respect to the true transmurality value $t_{s(i)}$ (with $s(i)$ the appropriate sector for the i-th measure):

$$LE^i = |\tilde{t}_{s(i)}^i - t_{s(i)}| \tag{32}$$

The behavior of ξ_s for the different methods is compared by means of the root mean square (RMSE) and the maximum error, both computed out of 100 experiments carried out with different scar configurations; results are shown in Table VII. In the basal sectors (1–4), Elnakib et al. achieved the best results, followed by Nazarian et al. and the 3D transmurality map method, whereas Schuijf et al. was the method with the highest error. However, the 3D transmurality map achieves better results in the mid-cavity and apical sectors, especially in the latter, where only 5 slices could be used by the 2D methods, since the rest of them contained no endocardial contour; however, the proposed method does not suffer from this limitation. This also leads to a high maximum error deviation of the 2D methods within these sectors, some as high as 0.782 in a measure that takes on values in $[0, 1]$, committed by Elnakib et al., while for the 3D transmurality map the maximum error was of 0.062. Taking into account all the sectors in the error computation, the 3D transmurality map achieved the best overall results.

Table VII

$RMSE = RMSE(\xi_s)$ AND $\xi_s^{\max} = \max(\xi_s)$) OF THE TRANSMURALITY ERROR BY SECTORS.

Sectors	Nazarian et al.		Schuijf et al.		Elnakib et al.		Prop. Upsampled	
	RMSE	$\xi_s^{\max}$	RMSE	$\xi_s^{\max}$	RMSE	$\xi_s^{\max}$	RMSE	$\xi_s^{\max}$
Basal	0.013	0.033	0.028	0.058	**0.005**	**0.021**	0.016	0.056
Mid-cavity	0.031	0.126	0.050	0.111	0.033	0.131	**0.011**	**0.048**
Apical	0.153	0.698	0.093	0.215	0.175	0.782	**0.021**	**0.062**
All	0.090	0.698	0.063	0.215	0.103	0.782	**0.016**	**0.062**

In order to check whether the model regularity affects performance, the phantom radii R_x and R_y had its length modified randomly a 20%, and their respective thicknesses D_x and D_y were also randomly changed 10% within each instance in which the transmurality was computed (see Figure 7(c)). In this case, each instance of RMSE is calculated from all the LE^i corresponding to the points within a myocardium at some selected slice and the magnitude we show is the average of RMSE along 100 experiments with different scar configurations. Results are shown in Figure 8. The vertical red and green dotted lines are located on the slices with a vertical transition of sectors in the endocardium and the epicardium, respectively. It may be observed that the 3D method provides transmurality measures in apical slices, while the other methods are unable to do so due to the reasons stated previously (i.e., no endocardium is found in them). We can see that in all the methods there are error peaks in the slices near the transition between basal and mid-cavity sectors, and between mid-cavity and apical sectors. For the proposed 3D method, the highest errors are located near the epicardial boundaries, while for the 2D methods they are in the slices with a mixture of basal and mid-cavity, or mid-cavity and apical sectors. Far from these transitions, where the scar has constant thickness, the proposed method with upsampling provides the least LE. Hence, geometry regularity seems important for the 2D methods to perform correctly.

The LE in the set of slices where all 2D and 3D methods could be applied (slices 1–50) was then inspected. In Figure 9, a box plot of the $RMSE(LE)$ values for the 100 trials with geometry variation shows that the 3D method with upsampling achieves the best results. We have also performed three two-sample t-tests —with significance

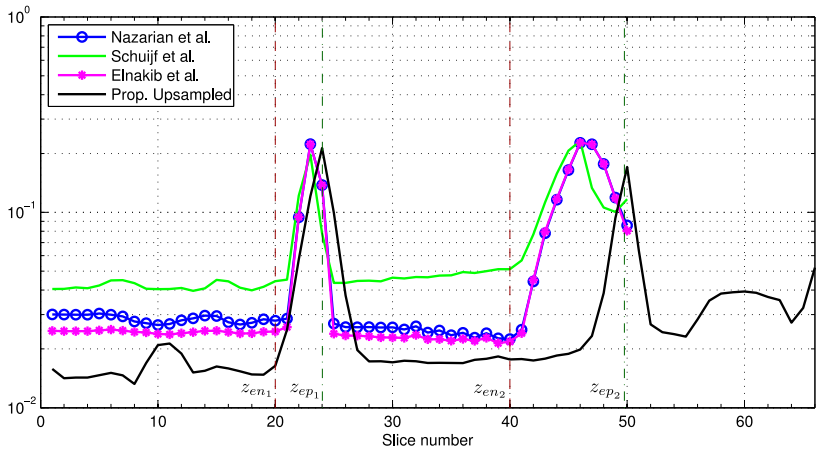

Figure 8. Average $RMSE(LE)$ within slices computed with different methods.

level of 0.05 assuming different variances— between the results of the 3D method with upsampling against those of each of the 2D methods. Results indicate that the mean of the $RMSE(LE)$ of the 3D method is smaller than the mean using any of the three other methods (for Nazarian et al. with $p < 10^{-20}$; using Schuijf et al., with $p < 10^{-29}$; and using Elnakib et al., with $p < 10^{-13}$).

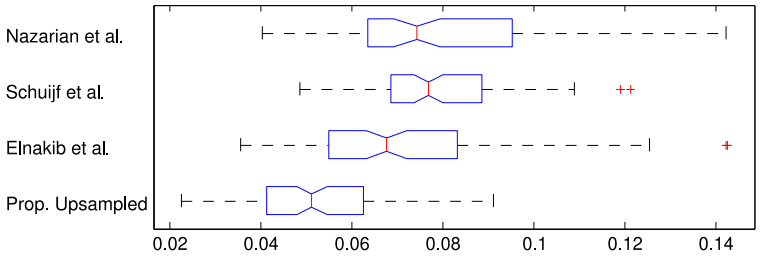

Figure 9. Box plots of the global $RMSE(LE)$ for the compared methods.

The slice orientation in short-axis acquisitions is manually done by the operator of the CMR equipment and may have a deviation with respect to the true short-axis orientation, with a subsequent volume rotation. In order to assess the effect that rigid transformations may have in the transmurality accuracy, we have conducted an experiment where the phantom with R_x=R_y=30, D_x=D_y=D_z=16 is rotated by a controlled pitch angle between 0 and 20° (see Figure 7(b)). To avoid favoring some sectors over others, a second rotation by a yaw angle is applied. Forty instances, each with a random yaw angle and scar configuration, were carried out for every pitch angle value.

The average global $RMSE(LE)$ by pitch angle is shown in Figure 10 for the proposed 3D method and Elnakib et al.'s algorithm, which achieved the best results among the 2D methods. The proposed 3D method achieves lower average $RMSE(LE)$ for every pitch angle. It may also be observed that the average error committed by Elnakib et al.'s method increases with the angle. With respect to the influence of the rigid transformation on the sector errors

ξ_s, Figure 11 shows the average $RMSE(\xi)$ for basal, mid-cavity and apical sectors. In the mid-cavity sectors both methods achieve similar results —slightly better for the proposed method, as shown in Figure 11(b)—, and in the apical sectors the local transmurality map method clearly yields a lower average error than Elnakib et al.' approach in the whole pitch angle range. In the basal sectors the error committed by Elnakib et al.'s method increases with the rotation angle, and has a higher error than the proposed 3D method for angles $\geq 10°$.

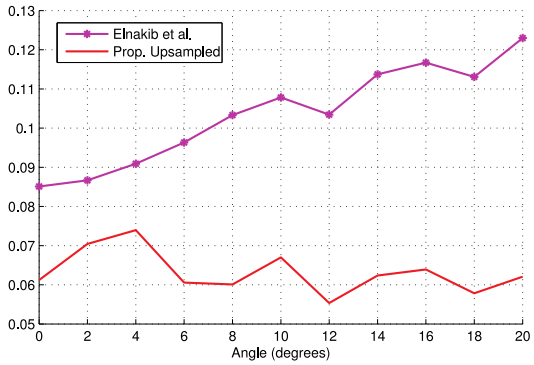

Figure 10. Average global $RMSE(LE)$ with respect to the pitch angle.

C. Transmurality Maps on Real Datasets

1) Image Dataset: Our dataset includes eight cardiac short axis CE-CMR volumes, acquired with a 1.5T GE Genesis Signa MRI scanner. Each of them has between 10 and 13 slices with 512×512 pixels and 10 mm of slice thickness. The in-plane spatial resolution varies among volumes, taking on values between 0.7031 mm and 0.9375 mm.

A set of endocardial and epicardial contours has been manually drawn for each volume by a cardiologist. To compute the scarred tissue masks $\chi_s[\mathbf{x}]$, the automatic segmentation method described in [32] has been used. Before computing the proposed 3D transmurality maps, the volumes of the dataset have been interpolated in the LA direction to provide nearly isotropic resolution using a registration-based interpolation method developed by our team [33].

2) Transmurality Maps on 2D slices: The transmurality map of three two-dimensional slices extracted from the CE-CMR volumes was computed. Figures 12(a), 12(d) and 12(g) show the myocardium with added endocardial (red), epicardial (green) and scar (yellow) contours. Both alternative transmurality maps $t(\mathbf{x})$ and $\hat{t}(\mathbf{x})$ are computed, the former appears in Figures 12(b), 12(e) and 12(h) and the latter in 12(c), 12(f) and 12(i). The $t(\mathbf{x})$ map shows the partial transmurality computed from the endocardium to $\mathbf{x}$, and thus provides the transmurality of the whole myocardial thickness at the epicardial nodes. The $\hat{t}(\mathbf{x})$ map assigns to $\mathbf{x}$ the transmurality computed in the streamline passing through that node, which discards information about the depth at which the non-viable tissue is located. The myocardial transmurality, however, is more easily visualized. Notice that in Figure 12(d) the largest scar island

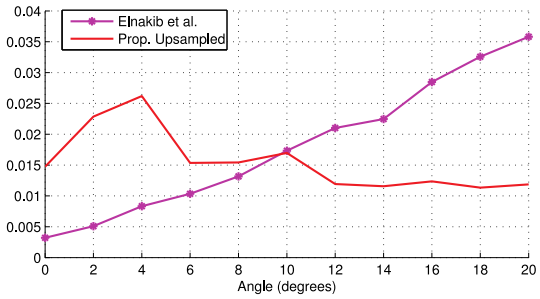

(a)

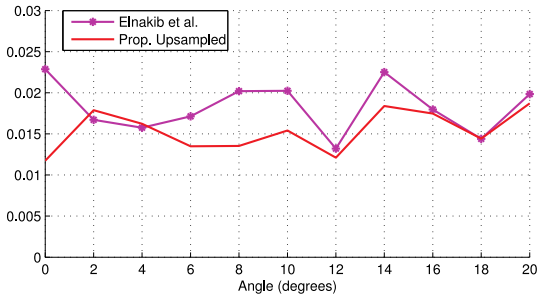

(b)

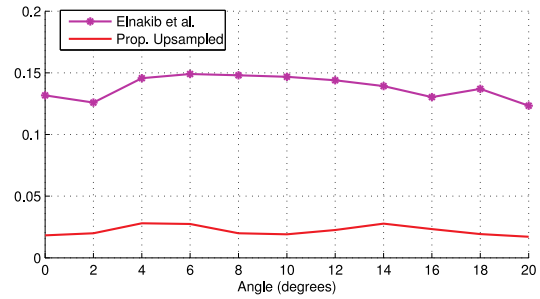

(c)

Figure 11. Average $RMSE(\xi)$ with respect to the pitch angle for all (a) basal, (b) mid-cavity, and (c) apical sectors.

is located near the epicardium. In that myocardium section, the local transmurality map (Figure 12(e)) is zero at the endocardium, and starts growing as it propagates through the non-viable tissue. In contrast, the local transmurality behavior when the scar is attached to the endocardium, as in 12(g), is to start with a unitary value at the endocardium which is maintained until healthy tissue is encountered, and then it begins decreasing as long as no new scar is crossed. These different behaviors makes the local transmurality map $t(\mathbf{x})$ provide information on the scar location, while $\hat{t}(\mathbf{x})$ does not.

3) 3D Transmurality Maps: Figure 13 shows renderings of the transmurality map computed on four interpolated CE-CMR volumes (where the endocardial and epicardial contours marked by experts have been interpolated accordingly) using the proposed three-dimensional method; as the visualization technique we have chosen an

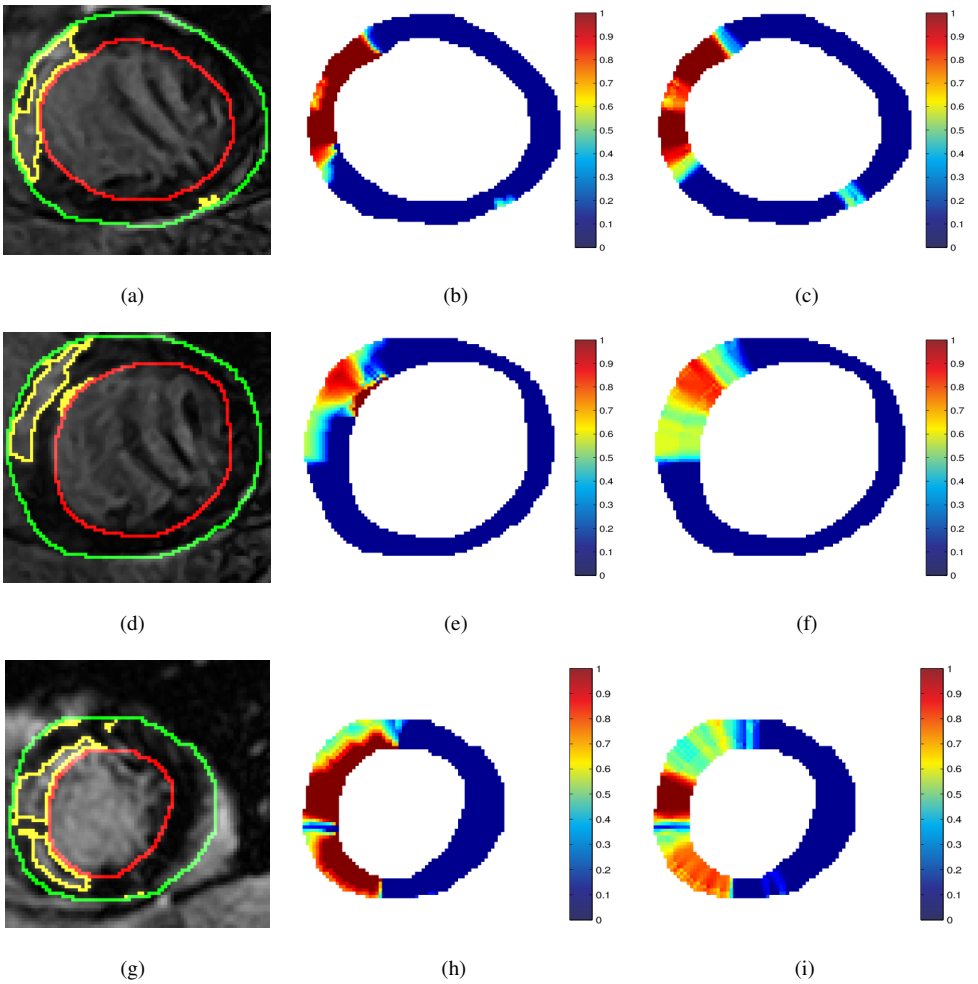

Figure 12. Examples on 2D CE-CMR slices, with the segmentation $s(\mathbf{x})$ on the left column ((a), (d) and (g)) and the transmurality maps $t(\mathbf{x})$ and $\hat{t}(\mathbf{x})$ on the central ((b), (e) and (h)) and right ((c), (f) and (i)) columns respectively.

epicardial isosurface where color maps the scar transmurality.

Figure 14 shows the projections of the isosurfaces at the isovalues $s(\mathbf{x}) = \{\frac{1}{3}, \frac{2}{3}, 1\}$ of the interpolated volume whose 3D rendering of the epicardial transmurality is shown in Figure 13(a), colored either by their transmurality (Figures 14(a), 14(e) and 14(i)) or by the associated scar segmentation (Figures 14(c), 14(g) and 14(k)). Three SA slices of the scar segmentation are included in Figures 14(d), 14(h) and 14(l). The bullseye diagram of the mean subendocardial transmurality at $s(\mathbf{x}) = \{\frac{1}{3}, \frac{2}{3}, 1\}$, computed after dividing the myocardium into sectors following [22] are displayed in Figures 14(b), 14(f) and 14(j). The angular offset θ_0 has been chosen so that the anterior (1, 7) and the anterolateral (6, 12) myocardial sectors are placed respectively at the leftmost and rightmost borders of the map, and sector numbers have been added to help locate any particular sector. Notice, however, that due to the 16 sector model design [22] and the choice of θ_0, a thin stripe from sector 13 experiences a wrap-around effect and appears at the rightmost border of the projection. It may be observed that regions with transmural scars have

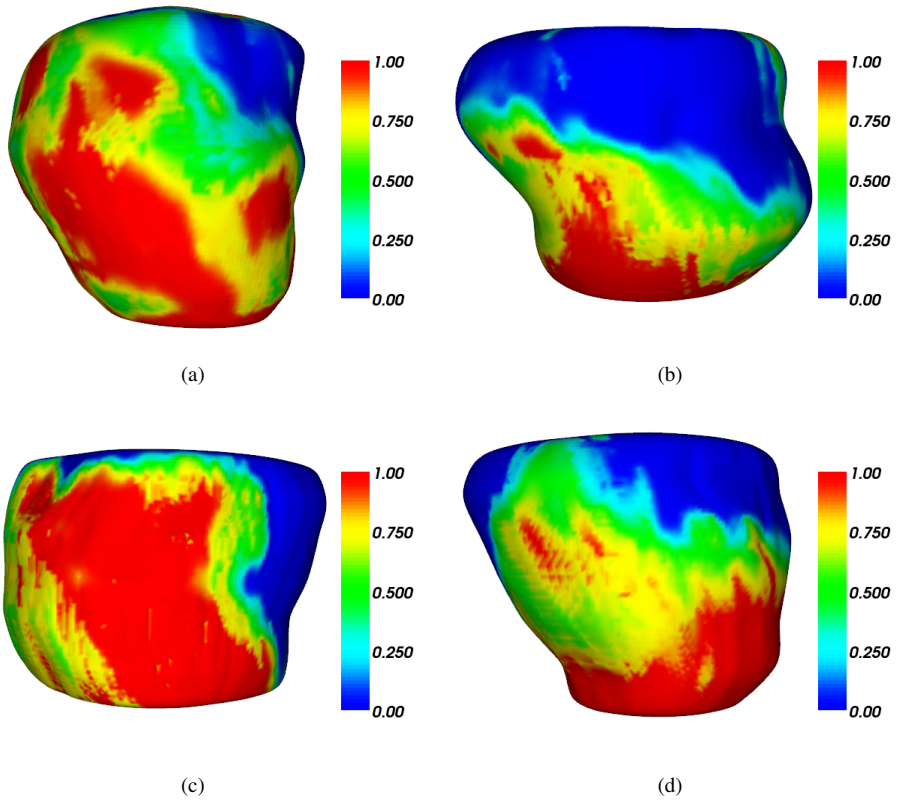

Figure 13. Three-dimensional transmurality maps at the epicardium of four interpolated CE-CMR volumes.

unitary transmurality in red color at every isovalue of $s(\mathbf{x})$ (see for example segments 8 and upper left corner of 14). Regions with subendocardial scar have a mostly unitary transmurality at low $s(\mathbf{x})$ values (near the endocardium), which decays at higher $s(\mathbf{x})$ values where no more scar is present (see upper right corner of segments 7 and 14). On the contrary, regions with subepicardial scar have low transmurality values at low $s(\mathbf{x})$ values, which increases with $s(\mathbf{x})$ when scarred tissue is met (see sector 10). In sector 4 at $s(\mathbf{x})=\{\frac{2}{3},1\}$, a small region with increased transmurality, whose scar has not appeared in the segmentation projections shown in Figures 14(c) and 14(g), is displayed. This is due to a thin scar island between $s(\mathbf{x})=\frac{1}{3}$ and $s(\mathbf{x})=\frac{2}{3}$ which has not been crossed by the 2D projections of the segmentation.

4) Comparison with 2D Transmurality Methods: Lastly, we compare the 3D transmurality map yielded by the proposed framework (Figure 15(d)) with the 3D rendering of the epicardium colored by the result of the 2D transmurality methods [11], [19], [20] (respectively in Figures 15(c), 15(a), and 15(b)), computed slice by slice in one of the interpolated CE-CMR volumes, whose scar segmentation is shown in Figure 14. We observe that Figures 15(a) and 15(b) are similar to each other but different from Figures 15(c) and 15(d). The reason for this is that the former measure the scar thickness as a segment length, and the latter either probe the points along the path [19] or compute a line integral. In a patient with IHD, where the ischemic wave moves from the endocardium to the epicardium, both measuring philosophies would provide similar results, but this example has healthy tissue

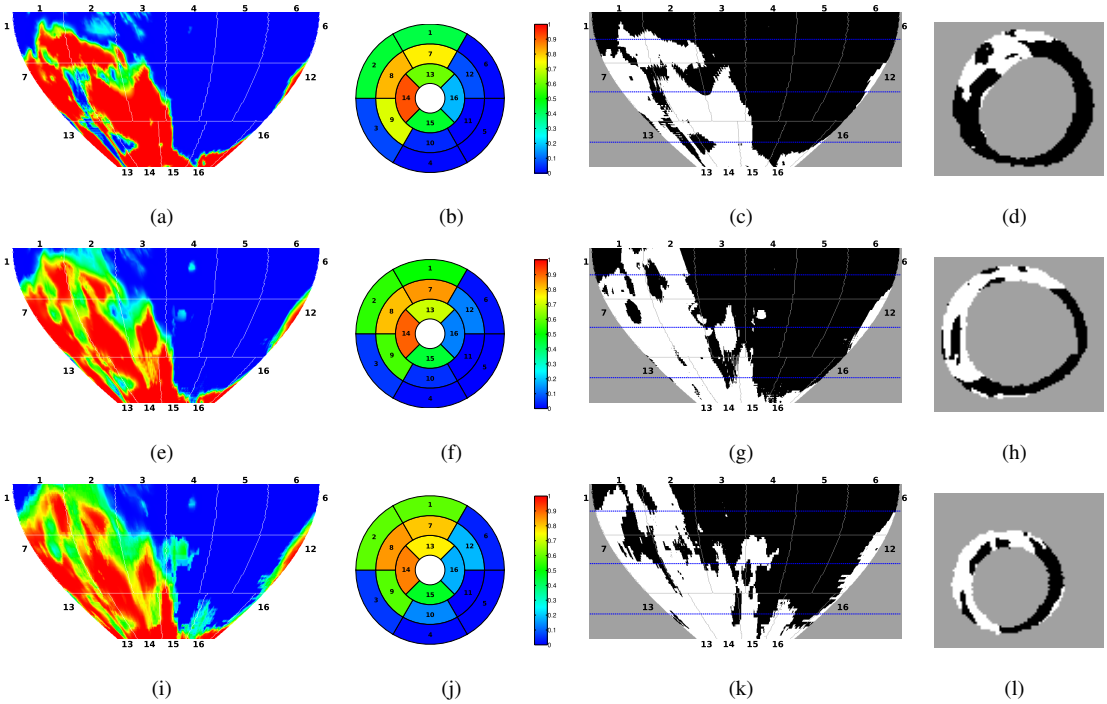

Figure 14. 2D projections of the local transmurality map rendered in Figure 13(a) at depths (a) $s(\mathbf{x})=\frac{1}{3}$, (e) $s(\mathbf{x})=\frac{2}{3}$, and (i) $s(\mathbf{x})=1$; with their respective bullseye diagrams in (b), (f) and (j). 2D projections of the associated scar segmentation at depths (c) $s(\mathbf{x})=\frac{1}{3}$, (g) $s(\mathbf{x})=\frac{2}{3}$, and (k) $s(\mathbf{x})=1$. Blue lines mark the crossings with the SA slices shown —from top to bottom— in (d), (h) and (l). Myocardial segments. (Basal) 1: Anterior, 2: Anteroseptal, 3: Inferoseptal, 4: Inferior, 5: Inferolateral, 6: Anterolateral. (Midventricular) 7: Anterior, 8: Anteroseptal, 9: Inferoseptal, 10: Inferior, 11: Inferolateral, 12: Anterolateral. (Apical) 13: Anterior, 14: Septal, 15: Inferior, 16: Lateral.

interlaced with scar (see Figure 14). It may also be seen how the proposed framework provides a smoother map than the 2D methods. The influence of allowing 3D point-to-point endocardial to epicardial matches can be appraised in the basal and apical regions of Figure 15(d). There, the streamlines respectively evolve upwards and downwards the LA direction (see Figure 5) due to the myocardial curvature, which translates into a stretched appearance along the LA compared to the 2D methods; particularly [19], shown in Figure 15(c).

VI. Conclusions and Future Work

A method for computing thickness and transmurality has been developed, which to our best knowledge is the first to be fully 3D. To this end, a MSSFM method has been created to compute line integrals along the streamlines of a scalar field gradient that fulfills a number of requirements. One such field is the harmonic function that arises from solving Laplace's equation within the myocardium. This method generalizes the one used in [24] for computing cortical and myocardial thickness and provides more accurate results thanks to a multi-stencil numerical scheme that has also been detailed. Using this method it is possible to compute scar thickness out of soft or hard segmentations and to provide a continuous framework for transmurality. We have also presented an algorithm to simultaneously build the myocardial and scar thickness. In addition to the transmurality being computed considering the whole myocardial thickness, this method also provides partial transmurality measures at any depth within the myocardium.

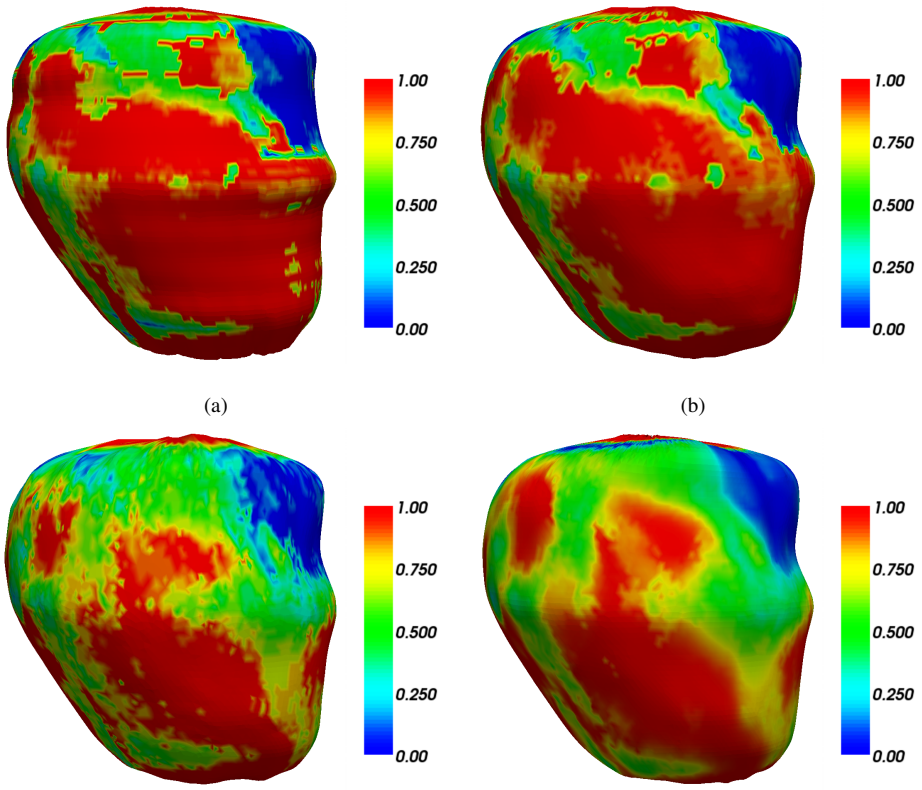

Figure 15. 3D transmurality maps of an interpolated CE-MRI volume, using the transmurality method proposed by: (a) Nazarian et al. [11], (b) Elnakib et al. [20], (c) Schuijf et al. [19], and (d) this paper.

The method has been tested on synthetic and real CE-CMR volumes. An experimental comparison of the accuracy of sector and local transmurality computed by existing 2D methods and the proposed framework shows that the 3D transmurality map is more robust against myocardial geometry deformations and rotations, performing better in mid-cavity and apical sectors. Additionally, it is capable of providing transmurality measures at the whole myocardium. This constitutes an advantage against 2D methods, which are unable to do so in apical slices where no endocardium is identified, but yet an endocardial-epicardial 3D correspondence may be established. We have also provided examples on how the location of the scarred tissue may be inferred from the transmurality map and have used a map projection technique to concurrently visualize the information contained at different depths of the 3D local transmurality. We plan to explore the application of local transmurality maps to other contrast enhanced MRI modalities.

REFERENCES

[1] W. H. Organization. The top 10 causes of death. Fact Sheet 310. http://www.who.int/mediacentre/factsheets/fs310/en/index.html. [Online]. Available: May2013

[2] ——. Cardiovascular diseases (CVDs). Fact Sheet 317. http://www.who.int/mediacentre/factsheets/fs317/en/index.html. [Online]. Available: May2013

[3] J. Schwitter, "Myocardial perfusion," *Journal of Magnetic Resonance Imaging*, vol. 24, no. 5, pp. 953–963, 2006.

[4] J. Vogel-Claussen, C. E. Rochitte, K. C. Wu, I. R. Kamel, T. K. Foo, J. A. C. Lima, and D. A. Bluemke, "Delayed Enhancement MR Imaging: Utility in Myocardial Assessment," *Radiographics*, vol. 26, no. 3, pp. 795–810, 2006.

[5] T. D. Karamitsos, J. M. Francis, S. Myerson, J. B. Selvanayagam, and S. Neubauer, "The role of cardiovascular magnetic resonance imaging in heart failure," *J Am Coll Cardiol*, vol. 54, no. 15, pp. 1407–1424, 2009.

[6] C. Parsai, R. O'Hanlon, S. K. Prasad, and R. H. Mohiaddin, "Diagnostic and prognostic value of cardiovascular magnetic resonance in non-ischaemic cardiomyopathies," *Journal of Cardiovascular Magnetic Resonance*, vol. 14, no. 54, pp. 1–24, 2012.

[7] P. G. Camici, S. K. Prasad, and O. E. Rimoldi, "Stunning, hibernation, and assessment of myocardial viability," *Circulation*, vol. 117, no. 1, pp. 103–114, 2008.

[8] A. Beek, O. Bondarenko, F. Afsharzada, and A. van Rossum, "Quantification of late gadolinium enhanced CMR in viability assessment in chronic ischemic heart disease: a comparison to functional outcome," *Journal of Cardiovascular Magnetic Resonance*, vol. 11, no. 1, p. 6, 2009.

[9] R. J. Kim, D. S. Fieno, T. B. Parrish, K. Harris, E.-L. Chen, O. Simonetti, J. Bundy, J. P. Finn, F. J. Klocke, and R. M. Judd, "Relationship of MRI Delayed Contrast Enhancement to Irreversible Injury, Infarct Age, and Contractile Function," *Circulation*, vol. 100, no. 19, pp. 1992–2002, 1999.

[10] R. J. Kim, E. Wu, A. Rafael, E.-L. Chen, M. A. Parker, O. Simonetti, F. J. Klocke, R. O. Bonow, and R. M. Judd, "The use of contrast-enhanced magnetic resonance imaging to identify reversible myocardial dysfunction," *New England Journal of Medicine*, vol. 343, no. 20, pp. 1445–1453, 2000.

[11] S. Nazarian, D. A. Bluemke, A. C. Lardo, M. M. Zviman, S. P. Watkins, T. L. Dickfeld, G. R. Meininger, A. Roguin, H. Calkins, G. F. Tomaselli, R. G. Weiss, R. D. Berger, J. A. C. Lima, and H. R. Halperin, "Magnetic resonance assessment of the substrate for inducible ventricular tachycardia in nonischemic cardiomyopathy," *Circulation*, vol. 112, no. 18, pp. 2821–2825, 2005.

[12] S. D. Roes, C. J. W. Borleffs, R. J. van der Geest, J. J. Westenberg, N. A. Marsan, T. A. Kaandorp, J. H. Reiber, K. Zeppenfeld, H. J. Lamb, A. de Roos, M. J. Schalij, and J. J. Bax, "Infarct Tissue Heterogeneity Assessed With Contrast-Enhanced MRI Predicts Spontaneous Ventricular Arrhythmia in Patients With Ischemic Cardiomyopathy and Implantable Cardioverter-Defibrillator / CLINICAL PERSPECTIVE," *Circulation: Cardiovascular Imaging*, vol. 2, no. 3, pp. 183–190, 2009.

[13] J.-M. Raymond, F. Sacher, R. Winslow, U. Tedrow, and W. G. Stevenson, "Catheter Ablation for Scar-related Ventricular Tachycardias," *Current Problems in Cardiology*, vol. 34, no. 5, pp. 225–270, 2009.

[14] A. Codreanu, F. Odille, E. Aliot, P.-Y. Marie, I. Magnin-Poull, M. Andronache, D. Mandry, W. Djaballah, D. Régent, J. Felblinger, and C. de Chillou, "Electroanatomic characterization of post-infarct scars: Comparison with 3-dimensional myocardial scar reconstruction based on magnetic resonance imaging," *Journal of the American College of Cardiology*, vol. 52, no. 10, pp. 839–842, 2008.

[15] E. Perez-David, A. Arenal, J. L. Rubio-Guivernau, R. del Castillo, L. Atea, E. Arbelo, E. Caballero, V. Celorrio, T. Datino, E. Gonzalez-Torrecilla, F. Atienza, M. J. Ledesma-Carbayo, J. Bermejo, A. Medina, and F. Fernández-Avilés, "Noninvasive Identification of Ventricular Tachycardia-Related Conducting Channels Using Contrast-Enhanced Magnetic Resonance Imaging in Patients With Chronic Myocardial Infarction: Comparison of Signal Intensity Scar Mapping and Endocardial Voltage Mapping," *Journal of the American College of Cardiology*, vol. 57, no. 2, pp. 184–194, 2011.

[16] A. Schmidt, C. F. Azevedo, A. Cheng, S. N. Gupta, D. A. Bluemke, T. K. Foo, G. Gerstenblith, R. G. Weiss, E. Marbán, G. F. Tomaselli, J. A. Lima, and K. C. Wu, "Infarct Tissue Heterogeneity by Magnetic Resonance Imaging Identifies Enhanced Cardiac Arrhythmia Susceptibility in Patients With Left Ventricular Dysfunction," *Circulation*, vol. 115, no. 15, pp. 2006–2014, 2007.

[17] A. T. Yan, A. J. Shayne, K. A. Brown, S. N. Gupta, C. W. Chan, T. M. Luu, M. F. Di Carli, H. G. Reynolds, W. G. Stevenson, and R. Y. Kwong, "Characterization of the Peri-Infarct Zone by Contrast-Enhanced Cardiac Magnetic Resonance Imaging Is a Powerful Predictor of Post-Myocardial Infarction Mortality," *Circulation*, vol. 114, no. 1, pp. 32–39, 2006.

[18] D. Andreu, A. Berruezo, J. T. Ortiz-Perez, E. Silva, L. Mont, R. Borras, T. Maria de Caralt, R. Jesus Perea, J. Fernandez-Armenta, H. Zeljko, and J. Brugada, "Integration of 3D Electroanatomic Maps and Magnetic Resonance Scar Characterization Into the Navigation System to Guide Ventricular Tachycardia Ablation," *Circulation: Arrhythmia and Electrophysiology*, vol. 4, no. 5, pp. 674–683, 2011.

[19] J. D. Schuijf, T. A. M. Kaandorp, H. J. Lamb, R. J. van der Geest, E. P. Viergever, E. E. van der Wall, A. de Roos, and J. J. Bax, "Quantification of myocardial infarct size and transmurality by contrast-enhanced magnetic resonance imaging in men," *American Journal of Cardiology*, vol. 94, no. 3, pp. 284–288, 2004.

[20] A. Elnakib, G. Beache, G. Gimel'farb, and A. El-Baz, "New automated Markov–Gibbs random field based framework for myocardial wall viability quantification on agent enhanced cardiac magnetic resonance images," *The International Journal of Cardiovascular Imaging (formerly Cardiac Imaging)*, vol. 28, no. 7, pp. 1683–1698, 2012.

[21] F. P. van Rugge, E. E. van der Wall, S. J. Spanjersberg, A. de Roos, N. A. Matheijssen, A. H. Zwinderman, P. R. van Dijkman, J. H. Reiber, and A. V. Bruschke, "Magnetic resonance imaging during dobutamine stress for detection and localization of coronary artery disease. quantitative wall motion analysis using a modification of the centerline method," *Circulation*, vol. 90, no. 1, pp. 127–138, 1994.

[22] American Heart Association Writing Group on Myocardial Segmentation and Registration for Cardiac Imaging:, M. D. Cerqueira, N. J. Weissman, V. Dilsizian, A. K. Jacobs, S. Kaul, W. K. Laskey, D. J. Pennell, J. A. Rumberger, T. Ryan, and M. S. Verani, "Standardized myocardial segmentation and nomenclature for tomographic imaging of the heart," *Circulation*, vol. 105, no. 4, pp. 539–542, 2002.

[23] S. E. Jones, B. R. Buchbinder, and I. Aharon, "Three-Dimensional Mapping of Cortical Thickness Using Laplace's Equation," *Human Brain Mapping*, vol. 11, pp. 12–32, 2000.

[24] J. Yezzi, A.J. and J. Prince, "An Eulerian PDE approach for computing tissue thickness," *IEEE Transactions on Medical Imaging*, vol. 22, no. 10, pp. 1332–1339, 2003.

[25] R. M. Setser, T. P. O'Donnel, N. G. Smedira, S. S. Halliburton, A. E. Stillman, and R. D. White, "Coregistered MR imaging myocardial viability maps and multi–detector row CT coronary angiography displays for surgical revascularization planning: Initial experience," *Radiology*, vol. 237, pp. 465–473, 2005.

[26] D. Peters, F. Liu, A. Tan, B. Knowles, H. Duffy, A. Wit, M. Josephson, and W. Manning, "Transmurality mapping of left ventricular scar: impact of spatial resolution," *Journal of Cardiovascular Magnetic Resonance*, vol. 13, no. Suppl 1, p. P163, 2011.

[27] C. Xu and J. L. Prince, "Snakes, shapes, and gradient vector flow," *IEEE Transactions on Image Processing*, vol. 7, no. 3, pp. 359–369, 1998.

[28] J. A. Sethian, "A fast marching level set method for monotonically advancing fronts," *Proceedings of the National Academy of Science*, vol. 93, no. 4, pp. 1591–1595, 1996.

[29] ——, *Level Set Methods and Fast Marching Methods: Evolving Interfaces in Computational Geometry, Fluid Mechanics, Computer Vision and Materials Science.* Cambridge University Press, 1999.

[30] M. S. Hassouna and A. A. Farag, "MultiStencils Fast Marching Methods: A Highly Accurate Solution to the Eikonal Equation on Cartesian Domains," *IEEE Transactions on Pattern Analysis and Machine Intelligence*, vol. 29, no. 9, pp. 1563–1574, 2007.

[31] S. Merino-Caviedes, L. Cordero-Grande, M. T. Pérez, and M. Martín-Fernández, "Transmurality Maps in Late Enhancement Cardiac Magnetic Resonance Imaging by a New Radial Fast Marching Method," in *XXIX Congreso Anual de la Sociedad Española de Ingeniería Biomédica*, Cáceres, Spain, 2011, pp. 211–214.

[32] Q. Tao, J. Milles, K. Zeppenfeld, H. J. Lamb, J. J. Bax, J. H. C. Reiber, and R. J. van der Geest, "Automated segmentation of myocardial scar in late enhancement MRI using combined intensity and spatial information," *Magnetic Resonance in Medicine*, vol. 64, no. 2, pp. 586–594, 2010.

[33] L. Cordero-Grande, G. Vegas-Sanchez-Ferrero, P. Casaseca-de-la Higuera, and C. Alberola-Lopez, "A Markov Random Field Approach for Topology-Preserving Registration: Application to Object-Based Tomographic Image Interpolation," *IEEE Transactions on Image Processing*, vol. 21, no. 4, pp. 2047–2061, 2012.